

Thermoelectric Figure of Merit of a Superatomic Crystal $\text{Re}_6\text{Se}_8\text{I}_2$ Monolayer


Tingwei Li¹, Peng-Hu Du¹, Ling Bai², Qiang Sun^{1,3,*} and Puru Jena⁴

¹*School of Materials Science and Engineering, Peking University, Beijing 100871, China*

²*Centre for Quantum Physics, Key Laboratory of Advanced Optoelectronic Quantum Architecture and Measurement (MOE), School of Physics, Beijing Institute of Technology, Beijing 100081, China*

³*Center for Applied Physics and Technology, Peking University, Beijing 100871, China*

⁴*Department of Physics, Virginia Commonwealth University, Richmond, Virginia 23284, USA*

 (Received 20 September 2022; revised 15 November 2022; accepted 16 November 2022; published 22 December 2022)

Superatomic materials are newly emerging candidates for high-performance thermoelectric (TE) devices due to their intrinsic ultralow thermal conductivities. However, the low TE power factor becomes a huge obstacle to reaching the required dimensionless figure of merit (ZT) values for practical applications. Here, motivated by the recently synthesized superatomic $\text{Re}_6\text{Se}_8\text{I}_2$ monolayer [He *et al.* *J. Am. Chem. Soc.* 144, 74 (2022)], we study its superior TE properties by using density functional theory combined with phonon Boltzmann transport theory and deep potential molecular dynamics. We show that the large mass and anharmonic Re—I bonds introduce strong phonon scattering and result in a low lattice thermal conductivity of $1.20 \text{ W m}^{-1} \text{ K}^{-1}$ at 300 K, while the strong and harmonic Re—Se network ensures a high TE power factor of $4344 \mu\text{W m}^{-1} \text{ K}^{-2}$ in the b direction for n -type doping. This is an order of magnitude higher than those of other cluster-based materials. Owing to the low thermal conductivity and high TE power factor, $\text{Re}_6\text{Se}_8\text{I}_2$ exhibits higher ZT values of 1.20 (500 K) and 1.43 (900 K) with n -type doping along the b direction compared with other cluster-based TE materials reported so far.

DOI: [10.1103/PhysRevApplied.18.064067](https://doi.org/10.1103/PhysRevApplied.18.064067)

I. INTRODUCTION

Modern industries dissipate over 60% of total energy as waste heat [1,2]. Confronting such huge energy dissipation, thermoelectric (TE) power generation provides an effective solution that enables a direct conversion of waste heat into useful electricity. The conversion efficiency of a TE device is mainly evaluated by the material's dimensionless TE figure of merit $ZT = S^2\sigma/(k_L + k_e)$. Thus, an ideal TE material, such as phonon-glass electron-crystal (PGEC) [3], should have a large Seebeck coefficient S , a high electrical conductivity σ , and a very low total thermal conductivity k , which is composed of the lattice thermal conductivity k_L and electronic thermal conductivity k_e . Note that the TE conversion efficiency is determined by the average ZT value over the target operating temperature range instead of the maximum value at one temperature T . However, the big challenge for realizing a high ZT value arises from the well-known trade-off relationship of S and σ via the concentration n . Besides, k_e is proportional to σ following the Wiedemann-Franz law [4]. Among these four transport parameters, k_L is the only term that is not

significantly affected by the others, thus providing an effective strategy to find TE materials with intrinsically ultralow lattice thermal conductivity.

On the other hand, the chemical bonding perspective offers an intuitive way to understand the origin of good TE properties [5,6], especially for low lattice thermal conductivity. According to the Slack's equation [7], materials with weak bonding strength, large average atomic mass, complex unit cell, and strong anharmonicity always exhibit low lattice thermal conductivity. Differing from atom-based materials with well-bonded structures, cluster-based materials [8] possess a unique structural type of chemical bonding hierarchy (CBH) with mixed weak bonds and strong bonds [9,10], where the weak bonds can induce special atomic vibrational motions with large asymmetric atomic displacement parameters [11]. These lead to a temperature-independent low lattice thermal conductivity, which enables high ZT values over a wide temperature range. In particular, the ability to change the size, symmetry, and chemical composition of clusters with atomic precision enables the design and synthesis of cluster-based materials to satisfy the other three characteristics mentioned previously, resulting in intrinsically ultralow lattice thermal conductivity [12–14].

Although cluster-based materials are of great advantage to realize ultralow thermal conductivity, the weakly

*sunqiang@pku.edu.cn

bonded atoms in the crystal structure also enhance the scattering of electrons and limit their TE performance. Until now, researchers have measured TE properties of some cluster-based materials assembled from C₆₀, B₁₂, GaS₄, GaSe₄, Mo₆Se₈, and Mo₉Se₁₁ clusters, as shown in Table I. It can be seen that the maximum ZT values of these cluster-based materials are all below 1, resulting in low conversion efficiency. According to the concept of PGEC, it is highly desirable to design materials with CBH having intrinsic channels for respectively conducting electrons and scattering phonons.

Here, we investigate the TE property of a newly synthesized two-dimensional (2D) hierarchical superatomic semiconductor Re₆Se₈I₂ [21], where the strong Re—Se covalent bonds offer electron transport channels, while the large asymmetric atomic displacement of I atoms in the Re—I bonds induce strong anharmonicity, thus, enhancing phonon scattering.

II. COMPUTATIONAL METHODS

A. Density functional theory calculations

All density functional theory (DFT) calculations are performed by using the Vienna *ab initio* simulation package (VASP) [22,23]. The projector-augmented-wave (PAW) method is used for all the atoms [24]. A vacuum layer of 12 Å along the c axis is set to avoid image interaction. A cutoff of 400 eV on the wave functions and a converged gamma-centered grid of k points in the Brillouin zone are used. For geometry optimization, both lattice and atom positions are fully relaxed until energy and force meet the convergence criteria of 10^{-8} eV and 10^{-6} eV/Å, respectively. Calculations are performed within the generalized gradient approximation (GGA) with the Perdew-Burke-Ernzerhof (PBE) exchange-correlation functional [25]. To get an accurate band gap, the Heyd-Scuseria-Ernzerh hybrid functional including spin-orbit coupling (HSE06 SOC) is used [26].

B. Electrical transport properties

The electrical transport properties are calculated using a combination of the HSE06 SOC band structure and Boltzmann transport theory [27] within the constant electron relaxation time approximation. A dense $15 \times 15 \times 1$ k -mesh is introduced in the irreducible Brillouin zone to obtain the converged transport properties such as the Seebeck coefficient S , electrical conductivity σ , and electronic thermal conductivity k_e . In BOLTZTRAP2, the core of calculations is the transport distribution (TD) function [28], which is defined as

$$\Xi(\varepsilon) = \sum_{\vec{k}} \mathbf{v}_{\vec{k}} \mathbf{v}_{\vec{k}} \tau_{\vec{k}}, \quad (1)$$

where $\mathbf{v}_{\vec{k}}$ and $\tau_{\vec{k}}$ are the group velocity and relaxation time at state k , respectively. Based on the TD function, S and σ are given by,

$$S = \frac{ek_B}{\sigma} \int d\varepsilon \left(-\frac{\partial f_0}{\partial \varepsilon} \right) \Xi(\varepsilon) \frac{\varepsilon - \phi}{k_B T}, \quad (2)$$

$$\sigma = e^2 \int d\varepsilon \left(-\frac{\partial f_0}{\partial \varepsilon} \right) \Xi(\varepsilon). \quad (3)$$

Here, e is the electronic elementary charge, k_B , f_0 , and ϕ are the Boltzmann constant, the Fermi-Dirac distribution function, and the chemical potential, respectively. The electronic thermal conductivity k_e is calculated by using the Wiedemann-Franz law,

$$k_e = L\sigma T, \quad (4)$$

where L is the Lorenz number, which is chosen to be 1.49×10^{-8} W Ω K⁻² for nondegenerate semiconductors [29,30].

The relaxation time τ and the carrier mobility μ for superatomic Re₆Se₈I₂ monolayer is estimated using Bardeen's deformation potential theory [31],

$$\tau = \frac{\mu m^*}{e} = \frac{m^*}{e} \frac{e\hbar^3 C^{2D}}{k_B T m^* m_d E_d^2} = \frac{\hbar^3 C^{2D}}{k_B T m_d^* E_d^2}, \quad (5)$$

where \hbar is reduced Planck's constant. m^* is effective mass of carriers in transport directions $a(m_a^*)$ and $b(m_b^*)$, and $m_d = (m_a^* m_b^*)^{1/2}$ is the density of states effective mass. C^{2D} and E_d represent the 2D elastic constant and deformation potential constant, respectively.

C. Lattice thermal conductivity

The lattice thermal conductivity k_L and phonon transport property calculations are carried out using the interatomic force constants (IFCs) as inputs and by solving the semiclassical phonon Boltzmann transport equation (PBTE) as implemented in the SHENGBTE code [32]. The second-order IFCs are estimated with a $3 \times 3 \times 1$ supercell as coded in the PHONOPY package [33]. The third-order IFCs are extracted with a converged cutoff distance of 7.6 Å and a supercell size of $3 \times 3 \times 1$, using the machine-learning-based HIPHIVE package [34,35]. The Born effective charges and dielectric constants are calculated to correct the long-range electrostatic interactions using density functional perturbation theory. We choose the buckling thickness plus the van der Waals radii of I atoms as the thickness (12.65 Å) in the k_L calculation.

TABLE I. Thermoelectric properties of some experimentally reported cluster-based materials.

Material	Cluster unit	Thermal conductivity ($\text{W m}^{-1} \text{K}^{-1}$), temperature (K)	Maximum ZT , temperature (K)	Ref.
FCC C_{60}	C_{60}	0.7, 300	0.12, 300	[15]
FCC K_3C_{60}	C_{60}	0.32, 300	0.29, 300	[15]
FCC K_6C_{60}	C_{60}	0.21, 300	0.53, 300	[15]
SmB_{62}	B_{12}	2.1, 300	0.13, 1050	[16]
$\text{Ag}_9\text{Ga}(\text{S}_{1-x}\text{Se}_x)_6$	$\text{GaS}_4\text{GaSe}_4$	<0.4 , 300–800	0.6, 800	[12]
$\text{Ag}_3\text{TI}_2\text{Mo}_{15}\text{Se}_{19}$	Mo_6Se_8 , $\text{Mo}_9\text{Se}_{11}$	1.5, 750	0.18, 750	[17]
$\text{Ag}_3\text{In}_2\text{Mo}_{15}\text{Se}_{19}$	Mo_6Se_8 , $\text{Mo}_9\text{Se}_{11}$	0.9, 300	0.45, 1100	[18]
$\text{K}_2\text{Mo}_{15}\text{Se}_{19}$	Mo_6Se_8 , $\text{Mo}_9\text{Se}_{11}$	2.0, 800	0.03, 800	[19]
$\text{Ag}_3\text{K}_2\text{Mo}_{15}\text{Se}_{19}$	Mo_6Se_8 , $\text{Mo}_9\text{Se}_{11}$	1.6, 800	0.18, 800	[19]
$\text{Ag}_x\text{Mo}_9\text{Se}_{11}$ ($3.4 \leq x \leq 3.9$)	$\text{Mo}_9\text{Se}_{11}$	0.8–1.2, 300	0.65, 800	[20]

D. Deep potential model

We train the interatomic potential for the $\text{Re}_6\text{Se}_8\text{I}_2$ monolayer using the deep potential molecular dynamics (DEEPM) method [36]. The training data set is prepared using the following steps: (1) We first generate 90 supercell structures containing 144 atoms by using the Monte Carlo rattle method in HIPHIVE. (2) For each configuration, we perform high-precision DFT calculations with a $3 \times 3 \times 1$ k -mesh for the supercell. (3) The atomic forces and total energy of the displaced systems are collected as a training data set for DEEPM training, where 80% of the data is used for training and 20% of the data for testing. The DEEPM training is set for 1 000 000 steps with good convergence (see Fig. S1(a) in the Supplemental Material [37]). We then use the deep potential (DP) model to calculate the phonon spectrum and compare with the results generated by PHONOPY and HIPHIVE (see Fig. S1(b) in the Supplemental Material [37]). These three nearly coincident curves establish the accuracy of DP.

III. RESULTS AND DISCUSSION

A. Structure and bonding

Unlike most 2D materials with atomic lattices, the $\text{Re}_6\text{Se}_8\text{I}_2$ monolayer is comprised of Re_6Se_8 superatomic building blocks, which is a 2D structural analogue of the 3D superconductor Chevrel phase [38,39]. As shown in Fig. 1(a), each superatomic cluster is connected to four neighbors by two Re—Se linkages in the basal plane and is capped by I atoms at the apical positions, forming a triclinic lattice with the $P-1$ (no. 2) space group. The primitive cell of the $\text{Re}_6\text{Se}_8\text{I}_2$ monolayer contains one Re_6Se_8 superatom and two I atoms, with lattice parameters $a = 6.678 \text{ \AA}$ and $b = 6.715 \text{ \AA}$. In a Re_6Se_8 superatomic cluster, the Re_6 octahedron is enclosed in a Se_8 cube. The hierarchical structure of the $\text{Re}_6\text{Se}_8\text{I}_2$ monolayer has two different types of bonds: one is a strong covalent bond between Re and Se atoms in intra- and inter- Re_6Se_8 superatoms, and the other is a relevantly weak bond between Re_6Se_8 superatoms and I atoms. To distinguish these two

different bonding mechanisms in an intuitive way, we choose two specific 2D planes from Fig. 1(a), and calculate their electron localization function (ELF) profile as shown in Fig. 1(b). It is a simple measure of electron localization in atomic and molecular systems related to the ratio of electron localization with respect to the uniform electron gas [40].

The ELF profiles reveal that electrons are distributed around Se and I atoms, but more localized around I atoms due to the larger electronegativity and stronger ability to accept electrons. The Bader effective charges are shown around the corresponding atoms in Fig. 1(b). Combining the ELF and Bader charge analysis, we conclude that Re—I bonds have a more ionic character, and the larger I ion results in a weaker Re—I bond, which would enhance the bond anharmonicity [41].

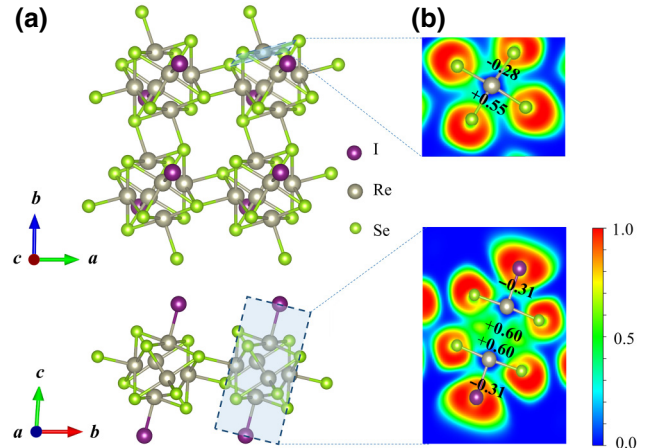


FIG. 1. (a) The top (upper) and side (bottom) view of $\text{Re}_6\text{Se}_8\text{I}_2$ monolayer, where Re, Se, and I atoms are represented by gray, green, and purple spheres, respectively. (b) ELF of $\text{Re}_6\text{Se}_8\text{I}_2$ monolayer. The specific 2D-slice projections are chosen to show the Re—Se (top) and Re—I (bottom) bonds. Bader effective charges are labeled around corresponding atoms.

B. Bonding strength and anharmonicity

The crystal orbital Hamilton population (COHP) analysis [42] allows us to quantify the bond strength by computing Hamilton-weighted populations of localized atomic orbitals. The COHP function is defined as $\text{COHP}_{ij}(E)$ and can be computed according to

$$\text{COHP}_{ij}(E) = H_{ij} \sum_n f_J c_{mi}^* c_{nj}^* \delta(E - E_n), \quad (6)$$

where f_j is the occupation number of each band j . H_{ij} represents the Hamiltonian matrix element between atomic orbitals φ_i and φ_j , and c_i and c_j are the coefficients of these atomic orbitals in the molecular orbital φ_n ($\varphi_n = \sum_i c_i^n \varphi_i$). A positive value for $-\text{COHP}_{ij}(E)$ symbolizes a bonding electronic interaction between the atomic orbitals i and j , whereas a negative value describes an antibonding interaction. The integrated COHP (ICOHP), which can measure the bond strength is also calculated. The $-\text{COHP}$ and ICOHP of Re—Se and Re—I atom pairs in the $\text{Re}_6\text{Se}_8\text{I}_2$ monolayer are shown in Fig. 2. The ICOHP value of Re—I bonding is -2.77 eV, which is more negative than that of Re—Se (-2.69 eV), illustrating that Re—Se atom pairs have more bonding states below the Fermi level, resulting in a stronger bond. On the other hand, the strength of atomic pair interactions can also be evaluated by the norm of second-order IFCs ($\phi_{ij}^{\alpha\beta}$). Firstly, we define the root mean square (RMS) of the element of the IFC tensor (Frobenius norm) as $\text{RMS } \phi_{ij} = \left[(1/9) \sum_{\alpha, \beta} (\phi_{ij}^{\alpha\beta})^2 \right]^{1/2}$, where $\phi_{ij}^{\alpha\beta}$ represents the harmonic response of the force acting on atom i (α direction) resulting from the displacement of atom j (β direction). Then, the RMS ϕ_{ij} with respect to the distance between atom i and atom j can be extracted and looped over all the atoms in a primitive cell to get insight into the interaction strength of different atom pairs. Based on the harmonic IFC analysis (see Fig. S2 in the Supplemental Material [37]), we demonstrate that the overall values of IFCs of Re—Se bonds are significantly larger than those of Re—I bonds, confirming the high interaction strength within the superatom and relatively low strength between superatom and I atom.

Generally, weak chemical bonds lead to large anharmonicity due to the large atomic displacements involved. Here, we try to illustrate the bonding anharmonicity by analyzing the *ab initio* molecular dynamics (AIMD) simulation trajectories. We perform two 5000-step AIMD simulations with a 2-fs time step in a $3 \times 3 \times 1$ supercell at 300 and 900 K, respectively. Trajectories of three random Re, Se, and I atoms are extracted and compared with their thermal displacements from the equilibrium position. Figure S3(a) in the Supplemental Material [37] shows that free energy fluctuates around a constant value and the final structure remains stable, confirming its thermal stability at 900 K. The MD trajectories at 300 and 900 K are shown

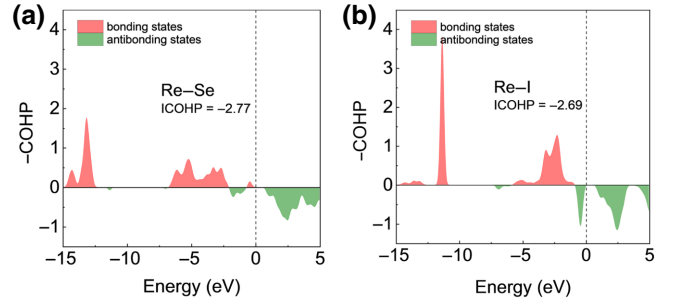


FIG. 2. COHP and ICOHP analysis of atom pairs of (a) Re—Se and (b) Re—I in $\text{Re}_6\text{Se}_8\text{I}_2$ monolayer. The bonding states and antibonding states are filled in red and green colors, respectively.

in Fig. 3. It can be seen that the displacements of Re and Se atoms are nearly isotropic around the equilibrium position at both 300 and 900 K, while the displacements of I atoms are strongly anisotropic at 300 K and become much larger at 900 K. Such large asymmetric displacements will enhance the lattice anharmonicity and enhance the phonon scattering process. The different features of MD trajectories between Re and Se atoms and I atoms correspond to two types of vibrations: the Re_6Se_8 superatom collectively rotates slightly in one direction and two I atoms vibrate widely in the opposite or same direction. The information about the thermal motions can also be obtained from the atomic displacement parameter, which measures the mean-squared displacements (MSDs) of an atom around its equilibrium position as a function of temperature. We compare the MSD parameter of the Re, Se, and I atoms along x , y , and z directions as shown in Fig. S4 in the Supplemental Material [37], which reveals that I atoms possess the largest MSD along the x and y directions; this is in agreement with the results of its MD trajectories. Based on this analysis, we can expect that the difference in bond strength between the Re—Se bond and Re—I bond would have a synergetic effect on the TE performance, where the weak and anharmonic Re—I bonds can enhance the phonon scattering and result in low lattice thermal conductivity, while the strong Re—Se network can ensure a high TE power factor.

C. Thermal transport properties

As shown in Fig. S3(b) in the Supplemental Material [37], the heavy Re and I atoms limit the cutoff frequencies of the acoustic phonon branches, where the cutoff frequency is defined as the maximum frequency in the linear part of the acoustic phonon branch [43]. The cutoff frequencies for the out-of-plane transverse acoustic (ZA) mode, transverse acoustic (TA) phonon mode, and longitudinal acoustic (LA) branches are less than 1 THz, which lead to low phonon group velocities. On the other hand, the localized vibrations of the I atoms contribute to almost

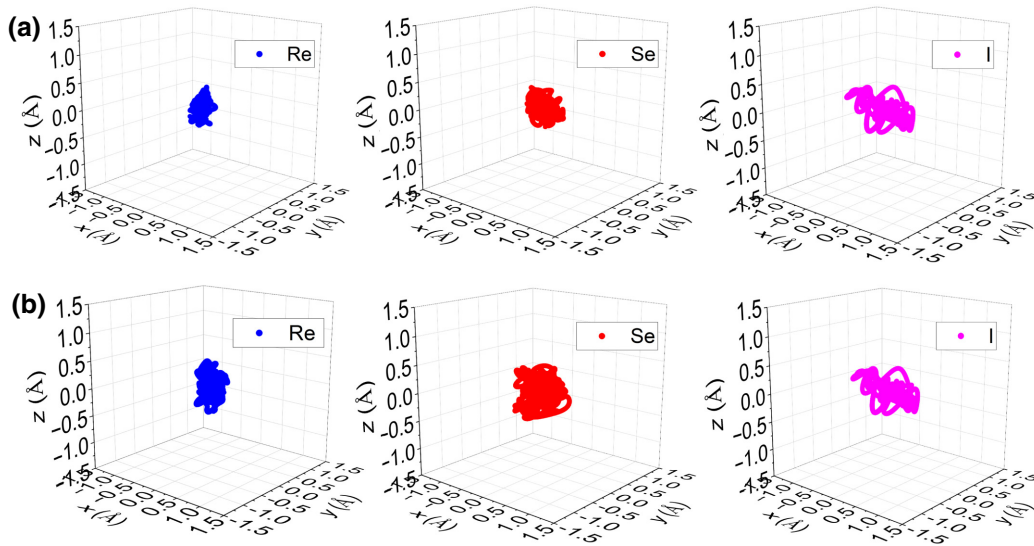


FIG. 3. The calculated three-dimensional MD trajectories of Re, Se, and I atoms in a 5000-step AIMD with 2-fs time step at (a) 300 K and (b) 900 K.

flat low-lying optical (LLO) phonon modes around 1 THz, which avoid crossing with the LA phonon mode as shown in the red circle (see Fig. S3(b) in the Supplemental Material [37]). It is well known that avoiding phonon crossing can reduce the lattice thermal conductivity by lowering the phonon group velocity and enhancing the phonon scattering rates [44]. Figures 4(a) and 4(b) show the results of phonon group velocity (v_g) and anharmonic scattering rates (Γ) of the $\text{Re}_6\text{Se}_8\text{I}_2$ monolayer at 300 K. As expected, LLO phonon branches exhibit ultralow v_g (approximately 1 km s^{-1}), and the v_g of the three acoustic phonon branches are all lower than 3.5 km s^{-1} , which are comparable to most of the state-of-art atom-based TEs [45,46]. Similarly, phonon modes with 1 THz frequency exhibit large Γ at 300 K and small phonon lifetimes, confirming the great anharmonicity induced by the large asymmetric displacements of I atoms. This large phonon anharmonicity, together with small group velocities and large phonon scattering processes, provides strong evidence of low lattice thermal conductivity in the superatomic $\text{Re}_6\text{Se}_8\text{I}_2$ monolayer.

Next, we calculate the temperature-dependent lattice thermal conductivity (k_L) of the $\text{Re}_6\text{Se}_8\text{I}_2$ monolayer. The results are plotted in Fig. 4(c). In the studied temperature range, the k_L values along the a and b directions are almost isotropic and yield a relation of $k_L \sim T^{-0.99}$. From 300 to 900 K, k_L exhibits very low values, dropping from 1.43 (1.48) to 0.48 (0.50) $\text{W m}^{-1} \text{K}^{-1}$ along the a (b) direction. The total thermal conductivity (k) is calculated as the sum of k_L and k_e , and the result is plotted in Fig. S5 (see in the Supplemental Material [37]). At room temperature (300 K), the thermal conductivities are 1.64 and 1.82 $\text{W m}^{-1} \text{K}^{-1}$ in the a and b directions for n -type doping, respectively. The corresponding values for p -type

doping are 1.50 and 1.58 $\text{W m}^{-1} \text{K}^{-1}$, indicating that the $\text{Re}_6\text{Se}_8\text{I}_2$ monolayer possesses low thermal conductivity. We further investigate the lattice thermal conductivity along the a direction at room temperature by using the reverse nonequilibrium molecular dynamics method with trained deep potential. The main idea behind this method is to develop a heat flux through the structure and obtain a temperature gradient along the heat flux direction. In detail, we first construct four models with lengths of 20.0, 26.7, 33.4, and 40.0 nm along the a direction by creating $m \times 6 \times 1$ ($m = 30, 40, 50, 60$) supercells. The periodic boundary condition is employed in the width direction to

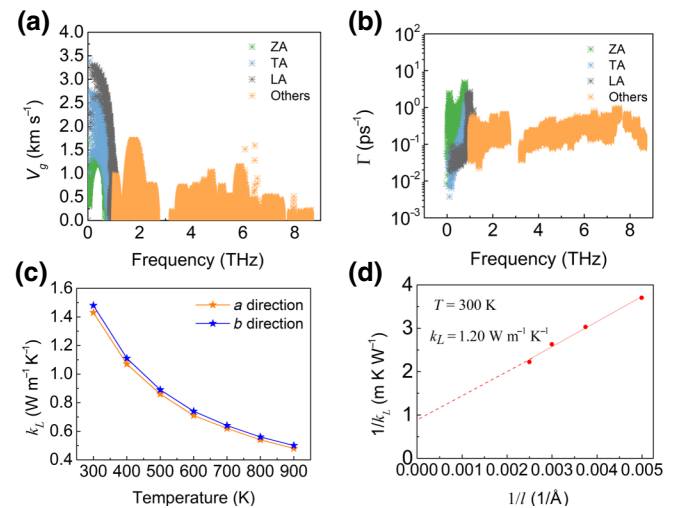


FIG. 4. (a) Group velocity (v_g), (b) anharmonic scattering rates (Γ), (c) lattice thermal conductivity (k_L), and (d) length-dependent lattice thermal conductivity of $\text{Re}_6\text{Se}_8\text{I}_2$ monolayer at 300 K. The dashed lines are linear fits to the discrete data.

TABLE II. Calculated carrier effective mass (m^*), deformation potential constant (E_d), 2D elastic constant, carrier mobility (μ), and carrier relaxation time (τ) of the $\text{Re}_6\text{Se}_8\text{I}_2$ monolayer at 300 K.

Direction	Carrier type	$m^*(m_0)$	E_d (eV)	C_{2D} (J m^{-2})	μ ($\text{cm}^2 \text{V}^{-1} \text{s}^{-1}$)	τ ($\times 10^{-14}$ s)
a	Hole	1.28	5.54	89.14	26.65	1.90
	Electron	1.58	4.26		29.96	2.68
b	Hole	5.22	5.21	85.12	7.05	2.08
	Electron	1.35	2.35		109.78	8.42

avoid the effect of the width dimension, while the fixed boundary condition is used in the heat transport direction. All models are relaxed by equilibrating in a NVT ensemble for 10 ns. After full relaxation, the system is switched to a NVE ensemble, and we apply the thermostats to the heat source and sink to obtain steady-state heat flux J by exchanging the kinetic energies between the heat source and sink for 1 ns. Then, the thermal conductivity can be derived from the ratio of heat flux and temperature gradient. As shown in Fig. 4(d), the lattice thermal conductivity increases almost linearly with length.

Such a significant size effect can be used to design nanostructures for further lowering the lattice thermal conductivity of the $\text{Re}_6\text{Se}_8\text{I}_2$ monolayer. By plotting $1/k_L$ vs $1/l$ [47] for a range of sample lengths and extrapolating to $1/l=0$ from a linear fit to the data, we predict the k_L of $\text{Re}_6\text{Se}_8\text{I}_2$ in the infinite length limit to be $1.20 \text{ W m}^{-1} \text{ K}^{-1}$ at 300 K. This leads to a reduction of 16% from the result of the PBTE method. Considering that the phonon mean free path of most acoustic phonon branches is larger than its minimum interatomic distance (2.55 \AA) in $\text{Re}_6\text{Se}_8\text{I}_2$ (see Fig. S6 in the Supplemental Material

[37]), we conclude that the contribution from diffusion-like phonons to k_L is negligible [48], and the four-phonon and other higher-order scattering processes contribute about $0.23 \text{ W m}^{-1} \text{ K}^{-1}$ to k_L in the superatomic $\text{Re}_6\text{Se}_8\text{I}_2$ monolayer at 300 K.

D. Thermoelectric properties

Besides thermal conductivity, chemical bonding can also affect the electronic band structure and TE properties. The band structures computed at the HSE06 SOC and PBE SOC level along with partial electron density of states are shown in Fig. S7 (see in the Supplemental Material [37]). The HSE06 SOC band structure gives an indirect band gap of $E_g = 1.45 \text{ eV}$ between the VBM at Γ ($0, 0, 0$) and the conduction band minimum (CBM) at Y ($0, 0.5, 0$). Compared with the results at the PBE SOC level, HSE06 SOC mainly affects the conduction band, upshifting the CBM energy by around 0.5 eV . From the results of the partial electron density of states, we can see that the CBM is related to the strong interactions between Re and Se atoms and exhibits a dispersive feature with smaller electron effective mass along the b direction. Based

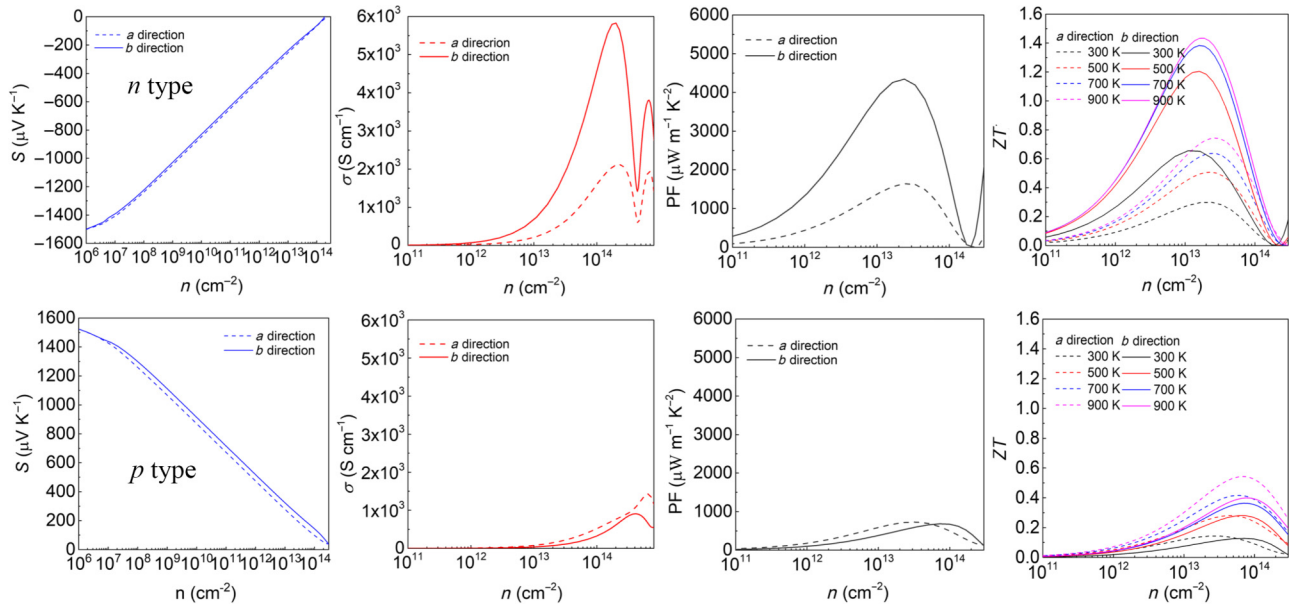


FIG. 5. Calculated Seebeck coefficient (S), electrical conductivity (σ), TE power factor (PF), and ZT values for n -type-doped and p -type-doped $\text{Re}_6\text{Se}_8\text{I}_2$ monolayer at 300 K.

TABLE III. The maximum TE power factor of the $\text{Re}_6\text{Se}_8\text{I}_2$ monolayer and other cluster-based materials at optimal doping.

Material	Cluster unit	TE power factor ($\mu\text{W m}^{-1} \text{K}^{-2}$), temperature (K)	Ref.
$\text{Re}_6\text{Se}_8\text{I}_2$	Re_6Se_8	4434, 300	This work
FCC C_{60}	C_{60}	300, 300	[15]
FCC K_3C_{60}	C_{60}	320, 300	[15]
FCC K_6C_{60}	C_{60}	410, 300	[15]
SmB_{62}	B_{12}	320, 1050	[16]
$\text{Ag}_9\text{Ga}(\text{S}_{1-x}\text{Se}_x)_6$	$\text{GaS}_4\text{GaSe}_4$	270, 800	[12]
$\text{Ag}_3\text{K}_2\text{Mo}_{15}\text{Se}_{19}$	$\text{Mo}_6\text{Se}_8\text{Mo}_9\text{Se}_{11}$	380, 800	[19]

on the carrier effective mass and other electronic transport results shown in Table II, the carrier mobility and relaxation time are calculated using the deformation potential theory. The $\text{Re}_6\text{Se}_8\text{I}_2$ monolayer exhibits the maximum relaxation time of 8.42×10^{-14} s and carrier mobility of $109.78 \text{ cm}^2 \text{ V}^{-1} \text{ s}^{-1}$ along the b direction for electrons, the latter being of the same order as that of some 2D transition-metal dichalcogenide semiconductors [49].

Next, we calculate the Seebeck coefficient (S), electrical conductivity (σ), and power factor (PF), defined as $\text{PF} = S^2\sigma$ with respect to carrier concentration along the a and b directions. The results are given in Fig. 5. Owing to the larger m_d of the hole, the peak value of S for p -type doping is slightly larger than that of n -type doping. These values are higher than those of PbTe (around $400 \mu\text{V K}^{-1}$) [50] and SnSe (around $530 \mu\text{V K}^{-1}$) [51] at 300 K, implying that both n - and p -type doping can produce a large TE effect. Apart from the Seebeck coefficients, electrical conductivities of the $\text{Re}_6\text{Se}_8\text{I}_2$ monolayer show anisotropy and strongly depend on the relaxation time (τ). The n -type-doped $\text{Re}_6\text{Se}_8\text{I}_2$ monolayer has the highest σ value because of the largest τ of electrons. The concomitant large S and high σ result in a peak PF value of $4344 \mu\text{W m}^{-1} \text{K}^{-2}$ in the $\text{Re}_6\text{Se}_8\text{I}_2$ monolayer along the b direction, which is an order of magnitude higher than those of other cluster-based materials (Table III).

Using these results of the electronic properties and the thermal conductivity, we calculate the figure of merit ZT ; the main results are given in Fig. 5. One can clearly see that n -type doping shows much better TE performance than p -type doping. At 300 K, the ZT value for the n -type doping along the b (a) direction is 0.65 (0.29), much higher than the corresponding value of 0.13 (0.14) for the p -type doping. Furthermore, the ZT value for the n -type $\text{Re}_6\text{Se}_8\text{I}_2$ can reach a value of 1.20 at 500 K and 1.43 at 900 K, which are the best values among the reported cluster-based materials, as shown in Table I.

IV. CONCLUSIONS

In summary, we investigate the TE properties of the recently synthesized superatomic $\text{Re}_6\text{Se}_8\text{I}_2$ monolayer by

using first-principles calculations combined with Boltzmann transport theory. We find that the $\text{Re}_6\text{Se}_8\text{I}_2$ monolayer possesses relatively low thermal conductivities ($<2 \text{ W m}^{-1} \text{K}^{-1}$) and high PF value of $4344 \mu\text{W m}^{-1} \text{K}^{-2}$ among all cluster-based TE materials. The heavy I atom with weak Re—I bond results in the large asymmetric atomic displacement and low cutoff of acoustic phonon frequencies, which enhance the phonon scattering process and reduce the phonon group velocity, thus leading to a low thermal conductivity. On the other hand, the strongly covalent-linked Re—Se network offers high carrier mobility for fast electrical transport. These features endow the superatomic $\text{Re}_6\text{Se}_8\text{I}_2$ monolayer with high ZT values of 1.20 at 500 K and 1.43 at 900 K along the b direction with optimal n -type doping. Our work clearly shows the promise of superatomic materials for TE applications.

ACKNOWLEDGMENTS

This work is partially supported by grants from the National Natural Science Foundation of China [Grant No. NSFC-21973001] and from the Ministry of Science and Technology of China [Grant No. 2017YFA0204902]. P.J. acknowledges partial support by the U.S. Department of Energy, Office of Basic Energy Sciences, Division of Materials Sciences and Engineering under Award No. DE-FG02-96ER45579. Calculations are performed on the High Performance Computing Platform of Peking University, China.

- [1] M. Zebarjadi, K. Esfarjani, M. S. Dresselhaus, Z. F. Ren, and G. Chen, Perspectives on thermoelectrics: from fundamentals to device applications, *Energy Environ. Sci.* **5**, 5147 (2012).
- [2] X. Zhang and L.-D. Zhao, Thermoelectric materials: Energy conversion between heat and electricity, *J. Materials* **1**, 92 (2015).
- [3] D. M. Rowe, *CRC handbook of thermoelectrics* (CRC press, Boca Raton, 1995).
- [4] R. Franz and G. Wiedemann, Ueber die Wärme-Leitungsfähigkeit der Metalle, *Ann. Phys.* **165**, 497 (1853).

- [5] Y. Yu, M. Cagnoni, O. Cojocaru-Mirédin, and M. Wuttig, Chalcogenide thermoelectrics empowered by an unconventional bonding mechanism, *Adv. Funct. Mater.* **30**, 1904862 (2020).
- [6] K. Tolborg and B. B. Iversen, Chemical bonding origin of the thermoelectric power factor in half-Heusler semiconductors, *Chem. Mater.* **33**, 5308 (2021).
- [7] G. A. Slack, in *Solid State Physics*, edited by H. Ehrenreich, F. Seitz, and D. Turnbull (Academic Press, New York, 1979), Vol. 34, pp.1–71.
- [8] P. Jena and Q. Sun, Super atomic clusters: Design rules and potential for building blocks of materials, *Chem. Rev.* **118**, 5755 (2018).
- [9] J. Nuss, U. Wedig, W. Xie, P. Yordanov, J. Bruin, R. Hübner, A. Weidenkaff, and H. Takagi, Phosphide–tetrahedrite $\text{Ag}_6\text{Ge}_{10}\text{P}_{12}$: Thermoelectric performance of a long-forgotten silver-cluster compound, *Chem. Mater.* **29**, 6956 (2017).
- [10] W. Lai, Y. Wang, D. T. Morelli, and X. Lu, From bonding asymmetry to anharmonic rattling in $\text{Cu}_{12}\text{Sb}_4\text{S}_{13}$ tetrahedrites: When lone-pair electrons are not so lonely, *Adv. Funct. Mater.* **25**, 3648 (2015).
- [11] T. Li, P.-H. Du, L. Bai, Q. Sun, and P. Jena, NaNO_3 monolayer: A stable graphenelike supersalt with strong four-phonon scattering and low lattice thermal conductivity insensitive to temperature, *Phys. Rev. Mater.* **6**, 064009 (2022).
- [12] S. Lin, W. Li, Z. Bu, B. Gao, J. Li, and Y. Pei, Thermoelectric properties of Ag_9GaS_6 with ultralow lattice thermal conductivity, *Mater. Today. Phys.* **6**, 60 (2018).
- [13] W.-L. Ong, E. S. O’Brien, P. S. M. Dougherty, D. W. Paley, C. Fred Higgs III, A. J. H. McGaughey, J. A. Malen, and X. Roy, Orientational order controls crystalline and amorphous thermal transport in superatomic crystals, *Nat. Mater.* **16**, 83 (2017).
- [14] A. Giri, S. S. Chou, D. E. Drury, K. Q. Tomko, D. Olson, J. T. Gaskins, B. Kaehr, and P. E. Hopkins, Molecular tail chemistry controls thermal transport in fullerene films, *Phys. Rev. Mater.* **4**, 065404 (2020).
- [15] J. Y. Kim and J. C. Grossman, Optimization of the thermoelectric figure of merit in crystalline C_{60} with intercalation chemistry, *Nano Lett.* **16**, 4203 (2016).
- [16] A. Sussardi, T. Tanaka, A. U. Khan, L. Schlapbach, and T. Mori, Enhanced thermoelectric properties of samarium boride, *J. Mater. Chem.* **1**, 196 (2015).
- [17] P. Gougeon, P. Gall, R. A. R. Al Orabi, B. Boucher, B. Fontaine, R. Gautier, A. Dauscher, C. Candolfi, and B. Lenoir, Electronic band structure and transport properties of the cluster compound $\text{Ag}_3\text{Ti}_2\text{Mo}_{15}\text{Se}_{19}$, *Inorg. Chem.* **58**, 5533 (2019).
- [18] P. Gougeon, P. Gall, R. A. R. Al Orabi, B. Fontaine, R. Gautier, M. Potel, T. Zhou, B. Lenoir, M. Colin, C. Candolfi, and A. Dauscher, Synthesis, crystal and electronic structures, and thermoelectric properties of the novel cluster compound $\text{Ag}_3\text{In}_2\text{Mo}_{15}\text{Se}_{19}$, *Chem. Mater.* **24**, 2899 (2012).
- [19] G. Daigre, P. Gougeon, P. Gall, O. Merdrignac-Conanec, R. A. R. Al Orabi, R. Gautier, A. Dauscher, C. Candolfi, and B. Lenoir, Unravelling the beneficial influence of Ag insertion on the thermoelectric properties of the cluster compound $\text{K}_2\text{Mo}_{15}\text{Se}_{19}$, *ACS Appl. Energy Mater.* **3**, 2846 (2020).
- [20] T. Zhou, B. Lenoir, M. Colin, A. Dauscher, R. A. R. Al Orabi, P. Gougeon, M. Potel, and E. Guilmeau, Promising thermoelectric properties in $\text{Ag}_x\text{Mo}_9\text{Se}_{11}$ compounds ($3.4 \leq x \leq 3.9$), *Appl. Phys. Lett.* **98**, 162106 (2011).
- [21] S. He, A. M. Evans, E. Meirzadeh, S. Y. Han, J. C. Russell, R. A. Wiscons, A. K. Bartholomew, D. A. Reed, A. Zangiabadi, M. L. Steigerwald, *et al.*, Site-selective surface modification of 2D superatomic Re_6Se_8 , *J. Am. Chem. Soc.* **144**, 74 (2022).
- [22] G. Kresse and J. Furthmüller, Efficient iterative schemes for ab initio total-energy calculations using a plane-wave basis set, *Phys. Rev. B* **54**, 11169 (1996).
- [23] G. Kresse and J. Furthmüller, Efficiency of ab-initio total energy calculations for metals and semiconductors using a plane-wave basis set, *Comput. Mater. Sci.* **6**, 15 (1996).
- [24] P. E. Blöchl, Projector augmented-wave method, *Phys. Rev. B* **50**, 17953 (1994).
- [25] J. P. Perdew, K. Burke, and M. Ernzerhof, Generalized Gradient Approximation Made Simple, *Phys. Rev. Lett.* **77**, 3865 (1996).
- [26] J. Heyd and G. E. Scuseria, Hybrid functionals based on a screened Coulomb potential, *J. Chem. Phys.* **118**, 8207 (2003).
- [27] G. K. H. Madsen, J. Carrete, and M. J. Verstraete, BoltzTraP₂, a program for interpolating band structures and calculating semi-classical transport coefficients, *Comput. Phys. Commun.* **231**, 140 (2018).
- [28] G. D. Mahan and J. O. Sofo, The best thermoelectric, *Proc. Natl. Acad. Sci. U. S. A.* **93**, 7436 (1996).
- [29] H.-S. Kim, Z. M. Gibbs, Y. Tang, H. Wang, and G. J. Snyder, Characterization of Lorenz number with Seebeck coefficient measurement, *APL Mater.* **3**, 041506 (2015).
- [30] X. Shi, J. Yang, J. R. Salvador, M. Chi, J. Y. Cho, H. Wang, S. Bai, J. Yang, W. Zhang, and L. Chen, Multiple-filled skutterudites: High thermoelectric figure of merit through separately optimizing electrical and thermal transports, *J. Am. Chem. Soc.* **133**, 7837 (2011).
- [31] J. Bardeen and W. Shockley, Deformation potentials and mobilities in non-polar crystals, *Phys. Rev.* **80**, 72 (1950).
- [32] W. Li, J. Carrete, N. A. Katcho, and N. Mingo, ShengBTE: A solver of the Boltzmann transport equation for phonons, *Comput. Phys. Commun.* **185**, 1747 (2014).
- [33] A. Togo and I. Tanaka, First principles phonon calculations in materials science, *Scr. Mater.* **108**, 1 (2015).
- [34] F. Eriksson, E. Fransson, and P. Erhart, The hiphive package for the extraction of high-order force constants by machine learning, *Adv. Theory Simul.* **2**, 1800184 (2019).
- [35] F. Pedregosa, G. Varoquaux, A. Gramfort, V. Michel, B. Thirion, O. Grisel, M. Blondel, P. Prettenhofer, R. Weiss, V. Dubourg, *et al.*, Scikit-learn: Machine learning in Python, *J. Mach. Learn. Res.* **12**, 2825 (2012).
- [36] H. Wang, L. Zhang, J. Han, and W. Ee, DeePMD-kit: A deep learning package for many-body potential energy representation and molecular dynamics, *Comput. Phys. Commun.* **228**, 178 (2018).
- [37] See Supplemental Material at <http://link.aps.org/supplemental/10.1103/PhysRevApplied.18.064067> for Deep Potential training loss, comparison of harmonic phonon spectra, norm of second-order interaction force constants, free energy, phonon spectra and phonon partial density of states, mean square displacements, total thermal conductivity,

- phonon mean free path, band structure at the level of Heyd-Scuseria-Ernzerh hybrid functional including spin-orbit coupling, and band structure at the level of Perdew-Burke-Ernzerhof exchange-correlation including spin-orbit coupling.
- [38] Ø Fischer, Chevrel phases: Superconducting and normal state properties, *Appl. Phys.* **16**, 1 (1978).
- [39] R. Chevrel, M. Hirrien, and M. Sergent, Superconducting Chevrel phases: Prospects and perspectives, *Polyhedron* **5**, 87 (1984).
- [40] A. D. Becke and K. E. Edgecombe, A simple measure of electron localization in atomic and molecular systems, *J. Chem. Phys.* **92**, 5397 (1990).
- [41] J. P. Heremans, The anharmonicity blacksmith, *Nat. Phys.* **11**, 990 (2015).
- [42] R. Nelson, C. Ertural, J. George, V. L. Deringer, G. Hautier, and R. Dronskowski, LOBSTER: Local orbital projections, atomic charges, and chemical-bonding analysis from projector-augmented-wave-based density-functional theory, *J. Comput. Chem.* **41**, 1931 (2020).
- [43] K. Pal, J. He, and C. Wolverton, Bonding hierarchy gives rise to high thermoelectric performance in layered Zintl compound BaAu₂P₄, *Chem. Mater.* **30**, 7760 (2018).
- [44] Y. Shen, F. Q. Wang, and Q. Wang, Ultralow thermal conductivity and negative thermal expansion of CuSCN, *Nano Energy* **73**, 104822 (2020).
- [45] Z. Rashid, A. Nissimagoudar, J. Ma, and W. Li, Phonon transport and thermoelectric properties of semiconducting Bi₂Te₂X (X = S, Se, Te) monolayers, *Phys. Chem. Chem. Phys.* **21**, 5679 (2019).
- [46] C. H. Lee, M. H. Ma, W. H. Li, P. C. Wei, Y. Y. Chen, Y. Zhao, and J. W. Lynn, Extremely space and time restricted thermal transport in the high temperature Cmc₂m phase of thermoelectric SnSe, *Mater. Today Phys.* **11**, 100171 (2019).
- [47] P. K. Schelling, S. R. Phillpot, and P. Keblinski, Comparison of atomic-level simulation methods for computing thermal conductivity, *Phys. Rev. B* **65**, 144306 (2002).
- [48] Y. Luo, X. Yang, T. Feng, J. Wang, and X. Ruan, Vibrational hierarchy leads to dual-phonon transport in low thermal conductivity crystals, *Nat. Commun.* **11**, 2554 (2020).
- [49] S. H. Mir, V. K. Yadav, and J. K. Singh, Recent Advances in the Carrier Mobility of Two-Dimensional Materials: A Theoretical Perspective, *ACS Omega* **5**, 14203 (2020).
- [50] L. Xu, Y. Zheng, and J.-C. Zheng, Thermoelectric transport properties of PbTe under pressure, *Phys. Rev. B* **82**, 195102 (2010).
- [51] L.-D. Zhao, S.-H. Lo, Y. Zhang, H. Sun, G. Tan, C. Uher, C. Wolverton, V. P. Dravid, and M. G. Kanatzidis, Ultralow thermal conductivity and high thermoelectric figure of merit in SnSe crystals, *Nature* **508**, 373 (2014).